Check for updates

Surface oxidation protection strategy of CoS$_2$ by V$_2$O$_5$ for electrocatalytic hydrogen evolution reaction†‡

Jie Wu,§[ab] Xuetao Qin,§[c] Yu Xia,§[de] Yuanyuan Zhang,[b] Bin Zhang,[b] Yunchen Du, [ID][b] Hsing-Lin Wang,*[d] Siwei Li [ID] *[bf] and Ping Xu [ID] *[b]

Transition metal sulfides (TMSs) are promising electrocatalysts for hydrogen evolution reaction (HER), while TMSs usually suffer from inevitable surface oxidation in air, and the impact of the surface oxidation on their HER catalytic activity remains unclear. Herein, we demonstrate an effective strategy for reducing the surface oxidation degree of easily oxidized CoS$_2$ by introducing glued vanadium pentoxide (V$_2$O$_5$) nanoclusters, taking advantage of the preferential adsorption and strong interaction between high-valence V and O$_2$. Combining oxidation protection and elaborate oxidation control experiments reveal that reduced surface oxidation degree of CoS$_2$ is conducive to affording promising HER catalytic performance, as the oxidized surface of CoS$_2$ can hinder the dissociation of water and thus is harmful to the HER process. Direct evidence is provided that surface oxidation should be carefully considered for TMS-based HER catalysts. The present work not only develops a new strategy for protecting CoS$_2$ from surface oxidation, but also provides deep insight into the impact of surface oxidation on the HER performance of transition metal compounds.

New concepts

Transition metal sulfides (TMSs) are important catalytic materials being widely used in the field of electrocatalysis, photocatalysis and thermal catalysis. Surface of TMSs can be easily oxidized under ambient conditions, however, the impact of the inevitable surface oxidation on the catalytic performance of TMSs has been always ignored. What's worse, efficient strategy for preventing TMSs from serious surface oxidation, crucial for academic and even industrial field, has not been developed. Herein, a novel strategy for preventing multiple TMSs from serious surface oxidation has been developed by introducing amorphous V$_2$O$_5$ clusters with close affinity to oxygen. Taking electrochemical hydrogen evolution reaction (HER) as a model reaction, the huge impact of the surface oxidation degree on the catalytic performance of TMSs has been shown clearly. We believe this work can not only arouse the attention on the surface oxidation of TMSs-based catalyst, but also provide a useful strategy for the surface protection of transition metal compounds including but not limited to TMSs.

[a] *National Engineering Laboratory for VOCs Pollution Control Technology and Equipment, School of Environment and Energy, South China University of Technology, Guangzhou 510640, China. E-mail: yhwj1105914174@foxmail.com*

[b] *MIIT Key Laboratory of Critical Materials Technology for New Energy Conversion and Storage, School of Chemistry and Chemical Engineering, Harbin Institute of Technology, Harbin 150001, China. E-mail: pxu@hit.edu.cn*

[c] *Beijing National Laboratory for Molecular Sciences, College of Chemistry and Molecular Engineering and College of Engineering, and BIC-ESAT, Peking University, Beijing 100871, China. E-mail: xuetaoqin@pku.edu.cn*

[d] *Department of Materials Science and Engineering, Southern University of Science and Technology, Shenzhen 518055, China. E-mail: wangxl3@sustech.edu.cn*

[e] *School of Physics and Astronomy, University of Birmingham, Edgbaston, Birmingham B152TT, UK. E-mail: 11856005@mail.sustech.edu.cn*

[f] *Institute of Industrial Catalysis, School of Chemical Engineering and Technology, Xi'an Jiaotong University, Xi'an 710049, China. E-mail: lisiwei@xjtu.edu.cn*

† Dedicated to the 120th anniversary of Southeast University.

‡ Electronic supplementary information (ESI) available: Fig. S1–S23. See DOI: https://doi.org/10.1039/d2nh00431c

§ These authors contributed equally to this work.

Introduction

Hydrogen evolution reaction (HER) is the cathodic reaction of water electrolysis, which is recognized as an important and sustainable approach to hydrogen production as clean fuels and chemical feedstocks.[1,2] Pt-based materials exhibit excellent activity for HER, but their high cost and scarcity limit the wide-spread applications.[3,4] Transition metal sulfides (TMSs) have been widely explored as a class of non-noble metal-based HER catalysts due to their unique physical and chemical properties.[5,6] Both layered MS$_2$ (*e.g.* MoS$_2$[7] and WS$_2$[8] and non-layered M$_x$S$_y$ (*e.g.* CoS$_2$,[9] FeS$_2$[10] and Ni$_3$S$_2$,[11] *etc.*) exhibit outstanding catalytic performance towards the HER, which are comparable or even superior to commercial Pt/C. Notably, multiple factors can impact the HER activity of TMSs, such as metal elements, ratios of metals and S atoms, vacancies, and electronic structures.[12,13] However, the impact of inevitable surface oxidation of TMSs on their HER performance has been paid less attention.

Like many TM compounds (*e.g.* carbides,[14,15] nitrides[16,17] and phosphides[18,19]), surface of TMSs can be easily oxidized under ambient conditions. In fact, the phenomenon that TMSs

are susceptible to surface oxidation has been widely discovered and reported for almost all kinds of TMSs, though the degree of surface oxidation depends on the kinds of metal and crystalline phase.[20–23] For example, surface oxidation degree of CoS_2 calculated based on X-ray photoelectron spectroscopy (XPS) increases from ~20% to ~90% only after 8 days exposure to air at room temperature.[24] In contrast, the surface oxidation degree of CoS_2, with the same metallic element as CoS_2, only increases from 10% to 20% under the same condition. Furthermore, the surface oxidation of MoS_2 is even too slight to be tested by some well-known surface sensitive characterization techniques such as XPS, which can only be detected by scanning tunneling microscopy.[20,24] To the best of our knowledge, most of the current works on this topic have not carefully considered the surface oxidation, and theoretical calculations based on the intrinsic TMS model are performed to explain the structure–performance relationship and catalytic mechanism. In our view, this is not rigorous for the easily oxidized TMSs (*e.g.* CoS_2).

Since the importance of surface oxidation of TMSs has not been paid enough attention, efficient strategy for preventing TMSs from serious surface oxidation, crucial for academic and even industrial field, has not been developed. High-valence early transition metals (*e.g.* V) have close affinity to O due to the characteristic of strong metal–O bonds,[25,26] and therefore can be used to stabilize the structure of the catalyst under the oxidative condition. Inspired by this strategy, herein we develop a new method for reducing the surface oxidation degree of easily oxidized CoS_2 by introducing glued V_2O_5 nanoclusters (marked as CoS_2–V_2O_5). The structure and surface oxidation degree of CoS_2 have been investigated by using electron microscopic and spectroscopic characterizations. Moreover, the impact of the surface oxidation degree of CoS_2 on the HER performance are explored through control oxidation experiments. This work provides a new method to protect the surface oxidation of TMS, and investigates the influence of the surface oxidation on the electrocatalytic HER performance of CoS_2.

Results

The synthesis process of CoS_2–V_2O_5 supported on carbon cloth (CC) is shown in Fig. 1. Firstly, CC supported Co zeolitic imidazolate frameworks (marked as Co MOFs) were immersed in Na_3VO_4 solution to get $Co_3V_2O_8$–Co MOFs intermediate *via* ion exchange process (Fig. S1–S7, ESI‡). Subsequently, the $Co_3V_2O_8$–Co MOFs was subjected to mild sulfidation at 400 °C under Ar atmosphere to obtain the CoS_2–V_2O_5 catalyst. The $Co_3V_2O_8$–Co MOFs intermediate with highly mixed Co and V elements may be a key factor for the generation of highly dispersed V_2O_5 nanoclusters around CoS_2. For comparison, the CoS_2 catalyst was synthesized *via* the same sulfidation treatment by directly using Co MOFs as the precursor (Fig. S8 and S9, ESI‡).

X-ray diffraction (XRD) was carried to study the structures of the as-synthesized samples (Fig. 2a). The XRD pattern of as-synthesized CoS_2 matches well with the standard cubic CoS_2
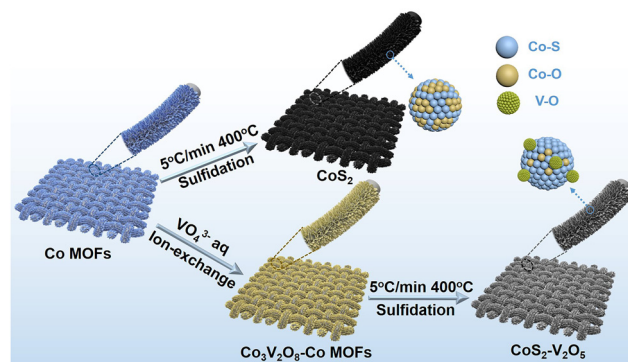

Fig. 1 Schematic illustration of the synthesis strategy of CoS_2 and CoS_2–V_2O_5 nanoarrays supported on carbon cloth (CC).

crystal phase (JCPDS No. 41-1471). However, for the V-incorporated CoS_2 sample, only diffraction peaks assigned to CoS_2 appear because V species cannot be detected by XRD due to low crystallinity and small particle size. The chemical composition of the V species was further investigated by using X-ray absorption fine structure (XAFS). The V K-edge X-ray absorption near-edge spectroscopy (XANES) of the as-synthesized sample is drastically similar to that of V_2O_5 (Fig. 2b), suggesting the formation of CoS_2–V_2O_5. Moreover, the bonding structures of V species were carried out by extend X-ray absorption fine structure (EXAFS, Fig. 2c). There are only V–O (1.56 Å) and
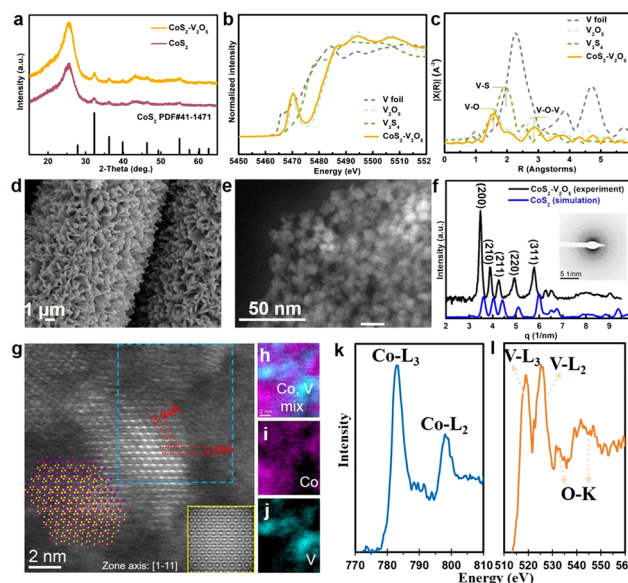

Fig. 2 Structural analysis of CoS_2–V_2O_5. (a) XRD patterns of CoS_2 and CoS_2–V_2O_5, (b) V K-edge XANES of CoS_2–V_2O_5, V foil, V_2O_5 and V_3S_4, (c) V K-edge EXAFS of CoS_2–V_2O_5, V foil, V_2O_5 and V_3S_4, (d) SEM image of CoS_2–V_2O_5 nanoarrays loaded on CC, (e) HAADF-STEM image of CoS_2–V_2O_5 particles, (f) radial intensity profile of CoS_2–V_2O_5 (black line) and the simulated radial intensity profile of CoS_2 (blue line), inset shows the SAED of CoS_2–V_2O_5, (g) atomic HAADF-STEM image of CoS_2–V_2O_5 along with the zone axis [1−11] direction (inset shows the atomic model of CoS_2), (h) cobalt and vanadium colormix, (i) cobalt mapping, (j) vanadium mapping, EELS spectra of k cobalt L edge, (l) oxygen K edge, and vanadium L edge acquired from the blue rectangular region in (g).

V–O–V (2.83 Å) scatterings in the V K-edge EXAFS spectra of CoS_2–V_2O_5, while the V–S scattering (1.97 Å) is absent. This is a direct evidence for the existence of vanadium oxides in the as-synthesized CoS_2–V_2O_5 heterostructure.

The morphology and crystallinity of the CoS_2–V_2O_5 heterostructure were further investigated by electron microscopy. The scanning electron microscopy (SEM) shows the similar nanoarray morphology to that of the Co MOFs precursor and $Co_3V_2O_8$–Co MOFs intermediate (Fig. 2d and Fig. S1, ESI‡). Upon closer observation by the high-angle annular dark-field scanning transmission electron microscopy (HAADF-STEM) image in Fig. 2e, the nanoarray grown on the carbon cloth consists of CoS_2–V_2O_5 nanoparticles that are about 8 nm in size. Notably, the integrated radial intensity profile (Fig. 2f) extracted from the selected area electron diffraction (SAED) corresponding to Fig. 2e is similar to the simulated radial intensity profile of CoS_2, where no peak can be attributed to V_2O_5, which indicates that the V_2O_5 is amorphous in nature.

Aberration corrected STEM and corresponding electron energy loss spectrum (EELS) were further employed to characterize the structure of CoS_2–V_2O_5. The atomic resolution image of CoS_2 is presented in Fig. 2g with the zone axis [1−11]. The measured lattice spacings of 3.94 Å and 3.86 Å indicate (110) and (0−11) planes with an angle of 120°. The simulated HAADF-STEM image of CoS_2 (110) facets with a d-spacing of 3.92 Å is presented at the bottom right corner of Fig. 2g, matching well with the atomic model of CoS_2 with (110) planes (inset in Fig. 2g).[27] More importantly, an area marked by the blue dashed rectangle in the STEM image was scanned for collecting the EEL spectra of V and Co elements to map the distribution of Co and V. As shown in Fig. 2h–j, Co and V elements were separated in space. Moreover, the low magnification mappings (Fig. S10, ESI‡) can also indicate that V_2O_5 was adhered on the surface of CoS_2 nanoparticles, with the size about 1–2 nm. As the amorphous V_2O_5 has been confirmed according to the previous characterizations, V_2O_5 nanoclusters (1–2 nm) are glued to the crystalline CoS_2 nanoparticles. The valence of V and Co were also analyzed from the EEL spectra (Fig. 2k–l). The peak intensity of V-L_3 (518.8 eV) is lower than that of V-L_2 (526.1 eV) with a ratio of $L_3/L_2 = 0.7$, indicating the valence of vanadium oxides in the as-synthesized sample is +5,[28] consistent to the XANES result. The calculated Co-L_3/L_2 ratio of 3 reveals that the valence of Co in the CoS_2 is a mixture of +2 and +3.[29]

Based on the above characterizations, the as-prepared CoS_2–V_2O_5 heterostructure is composed of crystalline CoS_2 nanoparticles around with amorphous V_2O_5 nanoclusters. The homogeneously distribution of V_2O_5 and CoS_2 at nanoscale is a key to the surface oxidation protection due to the formation of abundant CoS_2–V_2O_5 interfaces.

To demonstrate the surface oxidation protection effect of V_2O_5 nanoclusters, the surface oxidation degree of the CoS_2 and CoS_2–V_2O_5 samples is investigated by using spectroscopic characterizations and control experiments (Fig. 3). Raman spectrum of CoS_2 sample (Fig. 3a) shows peaks centered at ~487, 529, 600 and 698 cm^{-1} corresponding to the E_g, F_{2g}, F_{2g} and A_{1g}

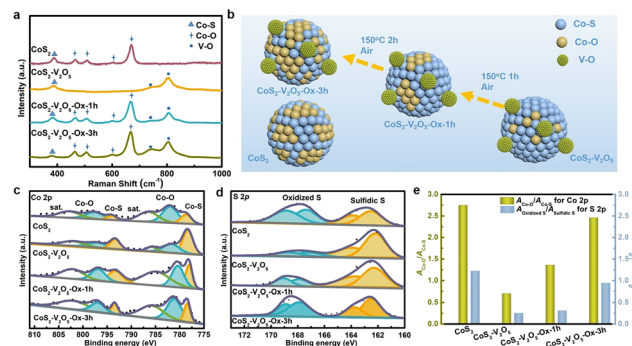Fig. 3 (a) Raman spectra of CoS_2, CoS_2–V_2O_5, CoS_2–V_2O_5-Ox-1h and CoS_2–V_2O_5-Ox-3h, in which Ox means a control oxidation process in Air at 150 °C, (b) schematic illustration of surface oxidation phenomenon of CoS_2, comparison of (c) Co 2p and (d) S 2p XPS spectra of CoS_2, CoS_2–V_2O_5, CoS_2–V_2O_5-Ox-1h and CoS_2–V_2O_5-Ox-3h, and (e) the ratios of $A_{Co–O} : A_{Co–S}$ and $A_{Oxidized\ S} : A_{Sulfidic\ S}$, in which A represents the peak area in the XPS spectra.

modes of Co–O species, respectively,[30] whereas the peak centered at 382 cm^{-1} is identified as the A_g mode of Co–S species.[31] The appearance of the Co–O species in the Raman spectrum have been reported to result from the surface oxidation of CoS_2 in air.[32] As seen from the Raman spectrum, the as-reported HER performance for CoS_2 has been heavily affected by the spontaneous surface oxidation, which may not reflect its catalytic activity. In contrast, the peaks assigned to Co–O species disappear in the Raman spectrum of the CoS_2–V_2O_5 sample. Instead, two peaks for V–O species (centered at 743 and 806 cm^{-1}) emerge along with the peaks for Co–S species.[33,34] This result implies that the surface oxidation degree of CoS_2 is significantly reduced upon the introduction of V_2O_5 nanoclusters.

Even though the CoS_2–V_2O_5 and CoS_2 catalysts have different surface oxidation degree, it is not enough to compare their HER performance to show the impact of surface oxidation. Therefore, we carried out a control oxidation experiments for the CoS_2–V_2O_5 (Fig. 3b) to obtain more control groups with different surface oxidation degree. Specifically, the CoS_2–V_2O_5 was oxidized in air at 150 °C for different time periods to tune the surface oxidation degree of CoS_2, which were marked as CoS_2–V_2O_5-Ox-1h and CoS_2–V_2O_5-Ox-3h, respectively. XRD patterns and SEM images of the control groups (Fig. S8 and S9, ESI‡) tell that the crystalline structures and morphologies of these oxidized samples almost keep unchanged. However, as seen in Fig. 3a, the four peaks assigned to Co–O peaks appear clearly in the Raman spectra of CoS_2–V_2O_5-Ox-1h and CoS_2–V_2O_5-Ox-3h, indicating that controlled surface oxidation of CoS_2 has been successfully realized.

XPS was further employed to investigate the surface oxidation degree of the above four samples. There are only Co, V (absent for the CoS_2 sample), O, S, C, and N elements in the survey spectra, indicating the purity of the as-synthesized samples (Fig. S11, ESI‡). In the V 2p spectra of the CoS_2–V_2O_5 and the oxidized samples, the peaks centered at 517.5 and 524.8 eV are assigned to V(+ 5) species (Fig. S12, ESI‡).[35] The Co 2p spectra of the samples can be divided into three couples of peaks (Fig. 3c). Specifically, the peaks centered at 778.7 and 794 eV are assigned

to the Co–S species, whereas the peaks at 782, 797.6, 786.5 and 803 eV are assigned to the Co–O species and the corresponding satellite peaks.[36] For the CoS_2 sample, the peak intensity of Co–O is relatively higher than that of Co–S, indicating the serious surface oxidation of CoS_2. The area ratio of Co–O and Co–S ($A_{Co–O}$: $A_{Co–S}$), which can reflect the surface oxidation degree of CoS_2, is calculated to be 2.75 for CoS_2. For $CoS_2–V_2O_5$, both Co–S and Co–O species can be detected in the Co 2p spectrum, because XPS is more sensitive to the surface species than Raman spectroscopy. The intensity of Co–O is much lower than that of Co–S and the value of $A_{Co–O}$: $A_{Co–S}$ decreases sharply to 0.7, a strong proof that the surface oxidation of CoS_2 is effectively reduced with the introduction of V_2O_5 nanoclusters. Furthermore, the peaks of Co–S for $CoS_2–V_2O_5$ are located at 778.18 and 793.08 eV, which are negatively shifted compared with CoS_2, suggesting the construction of $CoS_2–V_2O_5$ heterojunction structure. When the $CoS_2–V_2O_5$ is oxidized in air, the peak intensity of Co–O increases, while the peak intensity of Co–S decreases. The $A_{Co–O}$: $A_{Co–S}$ are calculated to be 1.36 and 2.46 for the $CoS_2–V_2O_5$-Ox-1h and $CoS_2–V_2O_5$-Ox-3h, respectively.

The above analyses based on the Co 2p spectra can be further supported by the S 2p spectra of these samples (Fig. 3d). In brief, both oxidized S and sulfidic S species can be found in all the S 2p spectra of CoS_2, $CoS_2–V_2O_5$, $CoS_2–V_2O_5$-Ox-1h and $CoS_2–V_2O_5$-Ox-3h, and the ratio of $A_{Oxidized S}$: $A_{Sulfidic S}$ is calculated to be 1.22, 0.25, 0.31 and 0.94, respectively, following the same trend as $A_{Co–O}$: $A_{Co–S}$ (Fig. 3e).

Three major conclusions about the surface oxidation of CoS_2 can be drawn according to the above Raman and XPS results. 1) As reported, CoS_2 suffers from serious surface oxidation in air. 2) Construction of the $CoS_2–V_2O_5$ hybrid materials can significantly reduce the surface oxidation degree of CoS_2. 3) The control oxidation experiment of $CoS_2–V_2O_5$ can tune the surface oxidation degree, which is helpful to understand the effect of surface oxidation on the HER performance of CoS_2.

The electrocatalytic performance of CC, commercial Pt/C, CoS_2, $CoS_2–V_2O_5$ as well as the control samples towards the HER was tested in alkaline media (1 M KOH). The reference electrode is calibrated experimentally (Fig. S13, ESI‡).[37] As shown in the iR-corrected linear sweep voltammetry (LSV, Fig. 4a) curves, bare CC shows very poor catalytic performance towards HER. The CoS_2 exhibits much better catalytic performance towards HER, requiring an overpotential of 272 mV to deliver a current density of 10 mA cm^{-2}. Significantly, once the $CoS_2–V_2O_5$ heterostructure is fabricated, the required overpotential is sharply reduced to 128 mV at 10 mA cm^{-2}. Moreover, $CoS_2–V_2O_5$ affords a mass activity of 0.71 A g^{-1} at an overpotential of 100 mV (Fig. S14, ESI‡), which is much higher than that of CoS_2 (0.18 A g^{-1}). Interestingly, when the $CoS_2–V_2O_5$ samples are oxidized for 1 h and 3 h, the HER performances drop gradually, requiring an overpotential of 166 and 196 mV at 10 mA cm^{-2}, respectively.

To further understand the impact of surface oxidation on the HER performance of CoS_2-based catalysts, we plot overpotential of the above $CoS_2–V_2O_5$ and CoS_2 catalysts as a function of the $A_{Co–O}$: $A_{Co–S}$ from XPS (Fig. 4b). For the
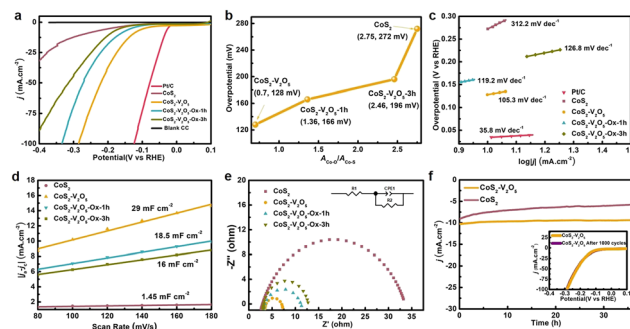

Fig. 4 HER performance of the as-prepared electrocatalysts in 1 M KOH solution. (a) LSV curves after iR correction in comparison to Pt/C, (b) the relationship between $A_{Co–O}/A_{Co–S}$ and the overpotential at 10 mA cm^{-2}, (c) Tafel plots, (d) C_{dl} extracting from the CV curves, (e) EIS spectra (inset shows the equivalent circuit used to simulate the Nyquist plots), and (f) long-time stability of $CoS_2–V_2O_5$ for 36 h (inset exhibits the LSV curves before and after 1000 CV cycles test).

$CoS_2–V_2O_5$ and $CoS_2–V_2O_5$-Ox samples, the overpotential increases almost linearly with surface oxidation degree from 128 to 196 mV, suggesting the surface oxidation degree is the dominant role for the different HER performance of these samples. The overpotential increases sharply for the CoS_2 catalyst (272 mV), implying that the V_2O_5 nanoclusters in the heterostructure may also contributes to the catalytic process. In sum, the lower surface oxidation degree of CoS_2, the better HER performance.

Furthermore, the HER kinetics of the CoS_2-based catalysts are informed from the corresponding Tafel plots in Fig. 4c. The Tafel slope of $CoS_2–V_2O_5$ is 105.3 mV dec^{-1}, which is smaller than that of CoS_2 (312.2 mV dec^{-1}), $CoS_2–V_2O_5$-Ox-1h (119.2 mV dec^{-1}) and $CoS_2–V_2O_5$-Ox-3h (126.8 mV dec^{-1}), indicating the facilitated reaction kinetics during HER process over $CoS_2–V_2O_5$. Additionally, electrochemical double layer capacitance (C_{dl}) is obtained from the cyclic voltammetry (CV) curves at different scan rates in the non-faradaic potential range (Fig. 4d and Fig. S15, ESI‡), which is an important parameter to derive the electrochemically active surface area (ECSA).[38] As the construction of $CoS_2–V_2O_5$ heterojunction structure, which is considered to effectively improve the capacitance performance[39,40] and as the more catalytical active sites (Co–S) are maintained due to the protection of V_2O_5, the $CoS_2–V_2O_5$ owns the highest ECSA (725 cm^2, Fig. S16, ESI‡). Thus, the $CoS_2–V_2O_5$ owns the highest C_{dl} (29 mF cm^{-2}) according to the equation ECSA = C_{dl}/C_s, in which C_{dl} is positively correlated to ECSA. As shown in Fig. S17 (ESI‡), we also conducted the turn over frequency (TOF) of CoS_2 and $CoS_2–V_2O_5$. The TOF values of CoS_2 and $CoS_2–V_2O_5$ are 0.13 s^{-1} and 0.08 s^{-1} at the overpotential of 150 mV, indicating the better intrinsic catalytic activity of $CoS_2–V_2O_5$, which is in accordance with C_{dl} and ECSA results. Moreover, as has been reported, the interface between CoS_2 and V_2O_5 can accelerate the kinetics of HER process and promote electron transport and finally reduce the charge transfer resistance.[41] Thus, the electrochemical impedance spectroscopy (EIS) for these samples suggests that the charge transfer resistance for $CoS_2–V_2O_5$ (3.86 Ω) is much smaller than that of CoS_2 (31.24 Ω),

CoS_2–V_2O_5-Ox-1h (9.87 Ω) and CoS_2–V_2O_5-Ox-3h (8.46 Ω) (Fig. 4e), demonstrating the enhanced charge transfer efficiency and improved reaction kinetics of CoS_2–V_2O_5 during the HER process. And CoS_2–V_2O_5 catalyst is also demonstrated to have an excellent mass transport property (Fig. S18, ESI‡). Besides, the HER Faraday efficiency (FE) of CoS_2 and CoS_2–V_2O_5 were performed under the current of 10 mA cm^{-2} for 6000 s, which were 98.1% and 98%, indicating the high selectivity during the HER process for both catalysts (Fig. S19, ESI‡).

The poor stability is a main drawback for CoS_2-based HER electrocatalyst. The chronoamperometric i–t curves at 10 mA cm^{-2} of CoS_2 and CoS_2–V_2O_5 were conducted for 36 h (Fig. 4f). There is significant degradation of current density of CoS_2, whereas the i–t curve of CoS_2–V_2O_5 keeps stable. It means the lower surface oxidation degree may also help to improve the stability of CoS_2-based HER catalyst. Moreover, the LSV curve of CoS_2–V_2O_5 after 1000 CV cycles basically coincides with the initial one (Fig. 4f, inset). Both experiments indicate the excellent long-term stability of the CoS_2–V_2O_5 catalyst towards HER. The excellent stability of CoS_2–V_2O_5 can be attributed to the well-maintained morphology and maintained Co–S surface, which is confirmed by using SEM, TEM and XPS (Fig. S20 and S21, ESI‡). We have also carried out Co K-edge XANES and EXAFS of CoS_2 and CoS_2–V_2O_5 after HER tests to understand the different stability of these two catalysts. Both XANES and EXAFS (Fig. S22, ESI‡) show CoS_2 converts to cobalt (hydr)oxides, which is consistent to the reported literatures.[23] In contrast, the Co–S and Co–S–V bonds in EXAFS clearly show that CoS_2 in the CoS_2–V_2O_5 catalyst retain stable after HER test, which is also supported by XPS result (Fig. S21, ESI‡). The V_2O_5 clusters can not only reduce the surface oxidation degree of CoS_2 in air, but also keep it stable during HER by avoiding the bulk oxidation. It is the structural stability of CoS_2–V_2O_5 that leads to the outstanding stability and long-term durability of this catalyst.).

Density functional theory (DFT) calculations were carried out to understand why the CoS_2 with lower surface oxidation degree exhibits better catalytic performance for HER. As shown in Fig. 5a–c, CoS_2 (100) and O modified CoS_2 (100) (marked as CoS_2–O) were selected as the models for simplification according to XRD results. Moreover, V_2O_5 clusters on CoS_2 (100) are built to represent the CoS_2–V_2O_5 sample. Generally, the elemental HER steps in alkaline solution include H_2O adsorption, H_2O activation, H desorption and OH desorption.[42,43] The chemisorption models of reaction intermediates adsorbed on the (100) surface of CoS_2 (*H_2O, *OH–H and *OH) are displayed concretely in Fig. S23 (ESI‡). The standard free energy (ΔG) diagrams for CoS_2 CoS_2–O and CoS_2–V_2O_5 of HER reaction steps are shown in Fig. 5d. For CoS_2, the Gibbs free energies of H_2O adsorption and H_2O dissociation are 0.37 and 0.67 eV, respectively, while the following steps are spontaneous. It can be learned that H_2O dissociation is the rate determining step (RDS) for CoS_2. With the CoS_2 surface modified by O, although the H_2O adsorption is effectively accelerated (ΔG = −0.05 eV), the energy barrier for H_2O dissociation is even higher, resulting in a much higher ΔG_{RDS} of 1.56 eV. The above results clearly show that the surface

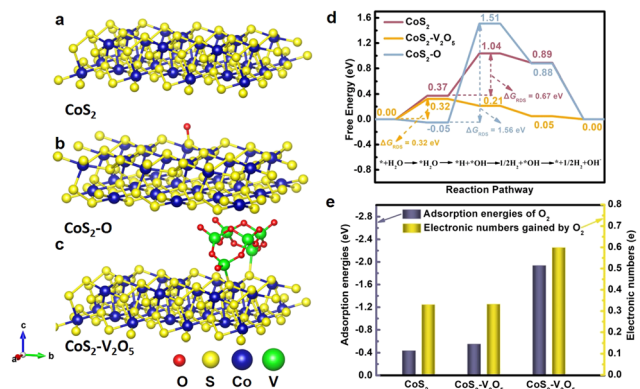**Fig. 5** (a–c) Crystal structures of CoS_2, CoS_2–O and CoS_2–V_2O_5, (d) comparison of standard Gibbs free energies at the rate determining step of CoS_2, CoS_2–O and CoS_2–V_2O_5 during the HER process, and (e) the adsorption energies of O_2 molecules at metal sites (Co sites and V sites) and the electronic numbers gained by O_2 molecules.

oxidation of CoS_2 is harmful to the HER process due to the hindering of H_2O dissociation.

We further investigate the synergetic effect of V_2O_5 and CoS_2 through DFT calculations. The contribution of V_2O_5 to HER is highlighted by comparing CoS_2 and CoS_2–V_2O_5 models (the red and yellow line, Fig. R6, ESI‡). The introduction of V_2O_5 will not bring an obvious change for H_2O adsorption, but it significantly accelerates the H_2O dissociation, leading to a spontaneous process (ΔG = −0.11 eV). As a result, the H_2O adsorption step becomes the RDS for CoS_2–V_2O_5, with a ΔG_{RDS} of 0.32 eV. The ΔG_{RDS} of CoS_2–V_2O_5 is lower than that of CoS_2, which means CoS_2–V_2O_5 possesses better catalytic activity for HER than CoS_2 from a theoretical point of view, matching well with the experimental results. Based on the theoretical calculations, the homogeneously distributed V_2O_5 can facilitate the dissociation of water and further the whole HER process. Therefore, the synergetic effect of V_2O_5 and CoS_2 include two parts. On one hand, V_2O_5 can reduce the surface oxidation of CoS_2 in air and the bulk oxidation of CoS_2 during HER, leading to exposed and stable Co–S sites for HER. On the other hand, V_2O_5 also contributes to the HER by facilitating the dissociation of water and further the whole HER process.

Another important issue is why the V_2O_5 nanoclusters can protect CoS_2 from surface oxidation. To answer this question, it is reasonable to investigate the adsorption and interaction between O_2 and the CoS_2 or CoS_2–V_2O_5 catalyst. V_2O_5 clusters on CoS_2 (100) were built to represent the CoS_2–V_2O_5 sample (Fig. 5c) and multiple theoretical methods were adopted. On one hand, the adsorption energy of O_2 molecule (E_{O_2}) on the CoS_2 (Co sites) and CoS_2–V_2O_5 (Co sites and V sites) was calculated (Fig. 5e, blue bar). E_{O_2} of Co site in CoS_2 is calculated to be −0.436 eV, meaning the adsorption of O_2 is spontaneously. By contrast, E_{O_2} of Co sites in the CoS_2–V_2O_5 is slightly reduced to −0.553 eV, which may result from the electronic interaction between the CoS_2 and V_2O_5 species. Significantly, E_{O_2} of V sites in the CoS_2–V_2O_5 reaches −1.935 eV, much lower than that of Co sites. The results clearly indicate that O_2

molecule preferentially adsorbs on V sites rather than Co sites in the CoS_2–V_2O_5. On the other hand, Bader charge analysis was applied to explore the charge transfer process between metal sites and adsorbed O_2 molecules (Fig. 5e, yellow bar). The number of the transferred electron is 0.330 for Co sites in CoS_2 and 0.332 and 0.559 for Co sites and V sites in CoS_2–V_2O_5. The more transferred electron, the stronger interaction between O_2 and metal sites. According to the above calculations, O_2 molecules in air can preferentially adsorb on V_2O_5 rather than CoS_2 and interact strongly with the V sites rather than Co sites in the CoS_2–V_2O_5 catalyst. As a result, the V_2O_5 nanoclusters protect the CoS_2 nanoparticles from serious surface oxidation.

Conclusions

In this work, we demonstrate a novel surface oxidation protection method for CoS_2 by introducing V_2O_5 nanoclusters, and systematically investigate the impact of surface oxidation on the HER performance. XAFS, HADDF-STEM and EELS demonstrate that amorphous V_2O_5 nanoclusters homogeneously glue to CoS_2 nanoparticles thanks to the MOFs-derived synthetic method, leading to significantly reduced surface oxidation degree of CoS_2 and excellent stability of CoS_2–V_2O_5 during HER by avoiding the bulk oxidation. The preferential adsorption and strong interaction between O_2 and V_2O_5 clusters help to protect CoS_2 from serious surface oxidation. As a result, CoS_2–V_2O_5 delivers a superior HER performance in alkaline media, requiring a low overpotential of 128 mV to deliver a current density of 10 mA cm^{-2}, which is much better than that of CoS_2 (272 mV). Through the control oxidation experiments of CoS_2–V_2O_5, it is demonstrated that the lower surface oxidation degree of CoS_2, the better HER performance. DFT calculations indicate that the surface oxidation of CoS_2 can hinder the dissociation of water, and the introduction of V_2O_5 can effectively facilitate the dissociation of water and further improve the HER process. This work shows the crucial impact of the surface oxidation of TMSs on their HER performance and provides a new idea for surface oxidation protection of CoS_2 that may be expanded to other TMSs and transition metal compounds.

Experimental section

Materials

Cobalt(II) nitrate hexahydrate ($CoNO_3 \cdot 6H_2O$), dimethyl imidazole ($C_4H_6N_2$), sodium orthovanadate (Na_3VO_4), sulfur powder (S), potassium hydroxide (KOH), iridium dioxide (IrO_2) and Nafion were all were purchased from Aladdin Industrial Corporation. Pt sheet was purchased from Aldrich. And deionized water (DI), absolute ethanol (C_2H_5OH). All chemicals were used directly without any purification treatment.

Methods

Synthesis of Co MOFs. In the synthesis of Co MOFs, 0.582 g $CoNO_3 \cdot 6H_2O$ and 1.314 g $C_4H_6N_2$ were dissolved in 40 mL of DI water, which were stirred for 15 minutes rapidly in order to mix evenly. Then, the solution of $C_4H_6N_2$ was quickly poured into the cobalt ion solution, which was stirred for again 5 minutes. After that, stop stirring and put the hydrophilic CC into the above mixed solution. After standing for 4 hours under the ambient conditions, the CC covered with blue Co MOFs was taken out, and then was washed by water, alcohol. Finally, drying it under vacuum overnight.

Synthesis of $Co_3V_2O_8$–Co MOFs. During the typical production of $Co_3V_2O_8$–Co MOFs, ion-exchange method was employed to etch the fresh Co MOFs. The specific method is as follows. Firstly, we prepared the etching solution by dissolving 0.3 g Na_3VO_4 in 60 mL of deionized water through a warm water bath. Subsequently, Co MOFs were put into the above solution. By adjusting the etching time, the samples of incompletely etched ($Co_3V_2O_8$–Co MOFs) and fully etched ($Co_3V_2O_8$) are obtained. The Co etching time for $Co_3V_2O_8$–Co MOFs was 20 minutes.

Synthesis of CoS_2–V_2O_5 and CoS_2. $Co_3V_2O_8$–Co MOFs were submitted to sulfidation at 400 °C with the heating rate of 5 °C min^{-1} under Ar inert atmosphere, producing CoS_2–V_2O_5. During the sulfidation process, 0.5 g S power was used as the sulfur source. Additionally, CoS_2 was also synthesized *via* the same sulfidation treatment only without the ion-exchange process.

Characterization. Rigaku D/MAXRC X-ray diffractometer (45.0 kV, 50.0 mA), equipped with the anticathode of Cu target, was used to collect XRD patterns. Quanta 200 S (FEI) and Tecnai F20 were used to take the scanning electron microscopic (SEM) and transmission electron microscopic (TEM) images, respectively. The X-ray energy dispersive spectroscopy (EDS) mappings were acquired by the microscope of FEI Talos™ F200X, working at 200 kV. The electron energy loss spectroscopy (EELS) was obtained under scanning transmission electron microscopy (STEM) mode at 300 kV using a Titan Themis G2 60-300 equipped with a monochromator and a probe corrector. The simulated STEM image of CoS_2 facets was generated using the kinematic scattering method, which is developed as a software running in Matlab. Before simulating, the atomic model of CoS_2 plane was built based on a cubic structure, whose space group is $Pa\bar{3}$. The software read the coordinates of Co and S atoms from the generated atomic model, creating the simulated image along with the direction of [1−11]. We used Renishaw in *Via* micro Raman spectroscopy system (laser wavelength: 532 nm) to record the Raman spectra. X-ray photoelectron spectra (XPS) were received by operating PHI 5700 ESCA system, in which an Al Kα radiation was used as a source ($h\nu$ = 1486.6 eV). The Fourier transform infrared spectroscopy (FT-IR) was received by operating with Tensor-27, Germany, Bruker system. The X-ray absorption fine structure spectra V K-edge were collected at 44A beamline of National Synchrotron Radiation Research Center (NSRRC) Taiwan.[44,45]

Electrode preparation and electrochemical measurements. Standard three-electrode system was carried to test the electrochemical performance of the as-prepared materials, in which the carbon rod, Hg/HgO and the electrode clip equipping with the catalysts were used as counter electrode, reference electrode

and working electrode, respectively. Furthermore, all the tests are carried out on CHI 660E workstation.

Theoretical calculations. At the DFT calculations part of this paper, the VASP software was conducted to perform the first-principles density functional theory calculation by the method of PAW.[46,47] In the calculation, the exchange functional is processed based on the PBE formula[48] and the generalized gradient approximation method.[49,50] The spin-polarized all results with a cut-off energy of 450 eV as the plane-wave basis set.

Conflicts of interest

There are no conflicts to declare.

Acknowledgements

References

1 B. Zhu, R. Zou and Q. Xu, *Adv. Energy Mater.*, 2018, **8**, 1801193.

2 J. Zhu, L. Hu, P. Zhao, L. Lee and K. Wong, *Chem. Rev.*, 2020, **120**, 851–918.

3 D. Liu, X. Li, S. Chen, H. Yan, C. Wang, C. Wu, Y. Haleem, S. Duan, J. Lu, B. Ge, P. Ajayan, Y. Luo, J. Jiang and L. Song, *Nat. Energy*, 2019, **4**, 512–518.

4 E. Kemppainen, A. Bodin, B. Sebok, T. Pedersen, B. Seger, B. Mei, D. Bae, P. Vesborg, J. Halme, O. Hansen, P. Lund and I. Chorkendorff, *Energy Environ. Sci.*, 2015, **8**, 2991–2999.

5 Y. Guo, T. Park, J. Yi, J. Henzie, J. Kim, Z. Wang, B. Jiang, Y. Bando, Y. Sugahara, J. Tang and Y. Yamauchi, *Adv. Mater.*, 2019, **31**, e1807134.

6 H. Sun, Z. Yan, F. Liu, W. Xu, F. Cheng and J. Chen, *Adv. Mater.*, 2020, **32**, e1806326.

7 Y. Yin, J. Han, Y. Zhang, X. Zhang, P. Xu, Q. Yuan, L. Samad, X. Wang, Y. Wang, Z. Zhang, P. Zhang, X. Cao, B. Song and S. Jin, *J. Am. Chem. Soc.*, 2016, **138**, 7965–7972.

8 L. Cheng, W. Huang, Q. Gong, C. Liu, Z. Liu, Y. Li and H. Dai, *Angew. Chem., Int. Ed.*, 2014, **126**, 7994–7997.

9 S. Peng, L. Li, X. Han, W. Sun, M. Srinivasan, S. Mhaisalkar, F. Cheng, Q. Yan, J. Chen and S. Ramakrishna, *Angew. Chem., Int. Ed.*, 2014, **126**, 12802–12807.

10 Y. Chen, S. Xu, Y. Li, R. Jacob, Y. Kuang, B. Liu, Y. Wang, G. Pastel, L. Salamanca, M. Zachariah and L. Hu, *Adv. Energy Mater.*, 2017, **7**, 1700482.

11 L. Feng, G. Yu, Y. Wu, G. Li, H. Li, Y. Sun, T. Asefa, W. Chen and X. Zou, *J. Am. Chem. Soc.*, 2015, **137**, 14023–14026.

12 C. Xie, D. Yan, H. Li, S. Du, W. Chen, Y. Wang, Y. Zou, R. Chen and S. Wang, *ACS Catal.*, 2020, **10**, 11082–11098.

13 T. Wang, H. Xie, M. Chen, A. Aloia, J. Cho, G. Wu and Q. Li, *Nano Energy*, 2017, **42**, 69–89.

14 C. Yang, H. Zhao, Y. Hou and D. Ma, *J. Am. Chem. Soc.*, 2012, **134**, 15814–15821.

15 S. Li, R. Cao, M. Xu, Y. Deng, L. Lin, S. Yao, X. Liang, M. Peng, Z. Gao, Y. Ge, J. Liu, W. Li, W. Zhou and D. Ma, *Natl. Sci. Rev.*, 2022, **9**, nwab026.

16 X. Yang, J. Nash, J. Anibal, M. Dunwell, S. Kattel, E. Stavitski, K. Attenkofer, J. Chen, Y. Yan and B. Xu, *J. Am. Chem. Soc.*, 2018, **140**, 13387–13391.

17 Y. Liu, D. Tian, A. Biswas, Z. Xie, S. Hwang, J. Lee, H. Meng and J. Chen, *Angew. Chem., Int. Ed.*, 2020, **59**, 11345–11348.

18 Z. Wu, X. Li, W. Liu, Y. Zhong, Q. Gan, X. Li and H. Wang, *ACS Catal.*, 2017, **7**, 4026–4032.

19 Y. Li, S. Li, J. Hu, Y. Zhang, Y. Du, X. Han, X. Liu and P. Xu, *J. Energy Chem.*, 2021, **53**, 1–8.

20 J. Peto, T. Ollar, P. Vancso, Z. Popov, G. Magda, G. Dobrik, C. Hwang, P. Sorokin and L. Tapaszto, *Nat. Chem.*, 2018, **10**, 1246–1251.

21 H. Liu, Z. Liu, F. Wang and L. Feng, *Chem. Eng. J.*, 2020, **397**, 125507.

22 Z. Yu, Y. Xie, B. Xie, C. Cao, Z. Zhang, H. Huo, Z. Jiang, Q. Pan, G. Yin and J. Wang, *Energy Storage Mater.*, 2020, **25**, 416–425.

23 W. Liu, E. Hu, H. Jiang, Y. Xiang, Z. Weng, M. Li, Q. Fan, X. Yu, E. Altman and H. Wang, *Nat. Commun.*, 2016, **7**, 10771.

24 Z. Wu, L. Huang, H. Liu, M. Li and H. Wang, *Nano Res.*, 2020, **14**, 2264–2267.

25 H. Sun, C. Tung, Y. Qiu, W. Zhang, Q. Wang, Z. Li, J. Tang, H. Chen, C. Wang and H. Chen, *J. Am. Chem. Soc.*, 2022, **144**, 1174–1186.

26 S. Li, C. Xi, Y. Jin, D. Wu, J. Wang, T. Liu, H. Wang, C. Dong, H. Liu, S. Kulinich and X. Du, *ACS Energy Lett.*, 2019, **4**, 1823–1829.

27 D. He, Z. Li and J. Yuan, *Micron*, 2015, **74**, 47–53.

28 S. Kalavathi, S. Amirthapandian, S. Chandra, P. Sahu and K. Sahu, *J. Phys.: Condens. Matter*, 2014, **26**, 015601.

29 Z. Wang and Y. Jiang, *Micron*, 2000, **31**, 571–580.

30 Z. Chen, L. Cai, X. Yang, C. Kronawitter, L. Guo, S. Shen and B. Koel, *ACS Catal.*, 2018, **8**, 1238–1247.

31 S. Lyapin, A. Utyuzh, A. Petrova, A. Novikov, T. Lograsso and S. Stishov, *J. Phys.: Condens. Matter*, 2014, **26**, 396001.

32 J. Li, Z. Xia, M. Zhang, S. Zhang, J. Li, Y. Ma and Y. Qu, *J. Mater. Chem. A*, 2019, **7**, 17775–17781.

33 P. Shvets, O. Dikaya, K. Maksimova and A. Goikhman, *J. Raman Spectrosc.*, 2019, **50**, 1226–1244.

34 P. Vilanova, J. Hernánde, A. Landa and F. Agulló, *J. Alloys Compd.*, 2016, **661**, 122–125.

35 S. Zhang, L. Zhang, G. Xu, X. Zhang and A. Zhao, *New J. Chem.*, 2020, **44**, 10918–10923.

36 X. Wang, X. Zhong, Z. Zha, G. He, Z. Miao, H. Lei, Q. Luo, R. Zhang, Z. Liu and L. Cheng, *Appl. Mater. Today*, 2020, **18**, 100464.

37 S. Niu, S. Li, Y. Du, X. Han and P. Xu, *ACS Energy Lett.*, 2020, **5**, 1083–1087.

38 J. Wu, Z. Yu, Y. Zhang, S. Niu, J. Zhao, S. Li and P. Xu, *Small*, 2021, **17**, e2105150.

39 R. Hu, Y. Liao, H. Qiao, J. Li, K. Wang, Z. Huang and X. Qi, *Ceram. Interfaces*, 2022, **48**, 23498–23503.

40 X. Wang, H. Li, H. Li, S. Lin, W. Ding, X. Zhu, Z. Sheng, H. Wang, X. Zhu and Y. Sun, *Adv. Funct. Mater.*, 2020, **30**, 1910302.

41 Y. Lin, K. Sun, S. Liu, X. Chen, Y. Cheng, W. Cheong, Z. Chen, L. Zheng, J. Zhang, X. Li, Y. Pan and C. Chen, *Adv. Energy Mater.*, 2019, **9**, 1901213.

42 L. Yu, I. Mishra, Y. Xie, H. Zhou, J. Sun, J. Zhou, Y. Ni, D. Luo, F. Yu, Y. Yu, S. Chen and Z. Ren, *Nano Energy*, 2018, **53**, 492–500.

43 W. Xu, N. Apodaca, H. Wang, L. Yan, G. Chen, M. Zhou, D. Ding, P. Choudhury and H. Luo, *ACS Catal.*, 2019, **9**, 5074–5083.

44 Z. Yu, H. Shan, Y. Zhong, X. Zhang and G. Hong, *ACS Energy Lett.*, 2022, **7**, 3151–3176.

45 Z. Yu, X. Zhang, C. Fu, H. Wang, M. Chen, G. Yin, H. Huo and J. Wang, *Adv. Energy Mater.*, 2021, **11**, 2003250.

46 G. Kress and J. Furthmuller, *Comput. Mater. Sci.*, 1996, **6**, 15–50.

47 G. Kress and J. Furthmuller, *Phys. Rev. B: Condens. Matter Mater. Phys.*, 1996, **54**, 11169.

48 J. Perdew, K. Burke and M. Emzerhof, *Phys. Rev. Lett.*, 1996, **77**, 3865.

49 G. Kresse and D. Joubert, *Phys. Rev. B: Condens. Matter Mater. Phys.*, 1999, **59**, 1758.

50 P. Blochl, *Phys. Rev. B: Condens. Matter Mater. Phys.*, 1994, **50**, 17953.